

Void-dynamics in nano-wires and the role of microstructure investigated via a multi-scale physics-based model

Cite as: J. Appl. Phys. **129**, 125102 (2021); <https://doi.org/10.1063/5.0039953>

Submitted: 08 December 2020 . Accepted: 07 March 2021 . Published Online: 24 March 2021

 A. S. Saleh,  H. Ceric, and  H. Zahednamesh



View Online



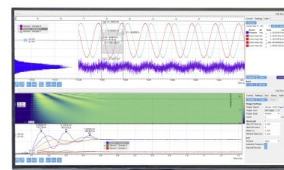
Export Citation



CrossMark

Challenge us.

What are your needs for
periodic signal detection?



Zurich
Instruments

Void-dynamics in nano-wires and the role of microstructure investigated via a multi-scale physics-based model

Cite as: J. Appl. Phys. **129**, 125102 (2021); doi: [10.1063/5.0039953](https://doi.org/10.1063/5.0039953)

Submitted: 8 December 2020 · Accepted: 7 March 2021 ·

Published Online: 24 March 2021



View Online



Export Citation



CrossMark

A. S. Saleh,^{1,2}  H. Ceric,³  and H. Zahednamesh^{1,a)} 

AFFILIATIONS

¹imec, Kapeldreef 75, B-3001, Leuven, Belgium

²Faculty of Engineering Sciences, KU Leuven, B-3001, Leuven, Belgium

³Institute for Microelectronics, TU Wien, Gußhausstraße 27-29/E360, 1040, Wien, Austria

^{a)}Author to whom correspondence should be addressed: Houman.Zahedmanesh@imec.be

ABSTRACT

With scaling of nano-interconnect linewidth toward a 3 nm technology node, electromigration in copper nano-interconnects is becoming a major limitation. In this context, the increase of texture polycrystallinity plays a major role and necessitates better understanding of the impact of void dynamics and its interaction with texture at operating conditions. To this end, comprehensive, yet efficient, physics-based numerical models are warranted given that electromigration experiments at low operating temperatures are not feasible. Albeit, development of such models has been a challenge since it involves large length-scale discrepancy between features, i.e., from wire dimensions (hundreds of micrometers) down to grains and voids (tens of nano-meters and below) leading to substantial computational cost. To this end, in this study an efficient multi-scale physics-based electromigration modeling approach is demonstrated, where an experimentally calibrated Korhonen-type 1D model solves electromigration at the global scale (entire interconnect), and a 2D local model simulates void dynamics considering the impact of electron wind, void surface energy, and stress gradients. The role of copper texture, i.e., grain boundaries, grain orientation and anisotropic properties is thoroughly investigated. We demonstrate that by tailoring the copper grain structure, void behavior and thus resistance evolution of nanowires can be effectively controlled. Compared to wider interconnects, in scaled nanowires, surface energy is found to play a dominant role on void morphology compared to electron wind. Strong anisotropy of diffusivity of copper's FCC lattice fosters faceted morphologies and emergence of slit morphology during void transition through the polycrystalline texture. Bamboo segments are shown to effectively pin the voids migrating toward the cathode in cases with cobalt cap. In addition, voids migrating from low diffusivity to high diffusivity regions adopt a longitudinally elongated morphology, which can be detrimental in a down-stream operation mode.

Published under license by AIP Publishing. <https://doi.org/10.1063/5.0039953>

I. INTRODUCTION

The understanding of the degradation of an interconnect metal due to the electromigration and the accompanying driving forces such as mechanical stress and temperature gradient is a demanding task. The degradation process involves redistribution of atoms inside the interconnect metal, which leads to the increase of mechanical stress.¹ Interconnect metal interfaces and the grain boundary network play a key role as fast diffusion paths.²

Since 1990s, copper has been by far the most important interconnect metal. The technology process, founded on copper, has been gradually refined and optimized in the past decades, leading to a mature fabrication process technology. However, degradation of copper

interconnects under operating conditions, particularly voiding, remains a major reliability issue which is aggravated with the downscaling of the interconnect width.^{3,4} The most widely used method for the investigation of failure induced by void formation in interconnects is by measurement of resistance under accelerated test conditions. Acceleration of failure dynamics is carried out by applying higher temperatures and higher current densities than intended for the normal operating conditions.⁵ The results of accelerated tests are used for standardized interconnect lifetime extrapolation, a method that comprises the application of Black's equation and lognormal properties of failure distribution.⁶

The physical modeling and simulation of the electromigration induced degradation of copper interconnect has been an

important part of the engineering of reliable interconnect structures.⁷ A particularly challenging part of electromigration modeling is the modeling of the dynamics of intrinsic voids in metals. The void dynamics includes void emergence, void growth, and void migration. Experimental insight into void dynamics can be obtained, for example, by *in situ* scanning electron microscopy (SEM), transmission electron microscopy (TEM) techniques, or by radiography (RT).^{8,9}

The physics of atomic migration along the void–metal interface has been well investigated and elaborated in numerous publications. Generally speaking, the normal velocity of a particular part of the void surface depends on the divergence of the atomic flux along the void surface, which is driven by electromigration (proportional to the tangential component of the electric field) and surface energy gradient (proportional to variation in temperature, stress, and curvature over the void surface). A multitude of numerical methods have been applied until now. At the beginning, numerical methods have utilized simple geometrical shapes of voids.¹⁰ Meanwhile also mathematically and computationally more demanding models based on the explicit FEM tracking^{11–13} of the void surface and on the level-set and phase field models^{14,15} have been utilized. More recent developments also include a successful application of cellular automaton algorithms.¹⁶ Even if the numerical modeling of void dynamics has been an active research field for several decades, there is still a gap between the sophisticated models and their application for practical engineering. The physical void dynamics models are usually presented and studied in a theoretical manner and for idealized cases rendering direct translation of the gained knowledge to practical reliability studies difficult. In this paper we present an approach which is well-founded on the state-of-the-art electromigration void physics and employs a multiscale numerical approach which allows for implementation of the corresponding models in such a way that a time-efficient detailed study of the technologically relevant failure scenarios is possible. In this context, there is a clear trend toward the increase in polycrystallinity with nano-wires due to dimensional down scaling.^{2,17} Considering the reliability impact of dimensional down-scaling as the grand challenge, we employ the developed model to generate further insight on the impact of copper texture and length-scale on void dynamics.

The paper is organized as follows: In Sec. II, a multi-scale modeling approach is presented which consists of the *global* and the *local* physical model. In Sec. III, the local physical model is discussed with regards to scaling effects and the prerequisite steps for the introduction of the numerical approach which is outlined in Sec. IV. In Sec. V, the wide applicability and true merits of the introduced modeling approach are illustrated in six tangible case studies based on realistic operating conditions. Finally, a direct comparison of simulation to experimentally observed void dynamics is illustrated.

II. METHODOLOGY

A. Multiscale physics-based modeling framework

A multiscale modeling approach is adopted whereby a modeling framework is developed in Matlab[®] that is composed of a global

module and a local module. The global module is based on the 1D Korhonen model which is applied over the entire length of the interconnect. The model resolves the total flux from the void based on the effective properties (i.e., Z^* , diffusivity) of the interconnect and as such is very efficient.¹⁶ The total flux from the void is then communicated to a local void dynamics module that is a 2D model with full details of the void, interconnect materials and grain structure and exhaustively resolves the void normal velocity based on the exact value of the tangent of current density on the void surface, surface tension, stress-distribution, and the total net flux resolved by the global module. This global-local approach (multi-scale) allows to take into account the impact of microstructure and all the stimuli on the void efficiently, whereby full detailed modeling is conducted at the local level in the critical cathode region and course graining is conducted at the global level over the entire length of the interconnect.

1. Global model

The electron wind force depletes the ions in the direction of the electron flow, while a back stress develops due to the compressive stress at the anode and drives ions in the opposite direction so that

$$J = -\frac{DC}{k_B T} \left(Z^* e E - \Omega \frac{d\sigma}{dx} \right), \quad (1)$$

where D is the diffusivity, C is the concentration, k_B is Boltzmann's constant, T is the temperature, Z^* is the effective charge number, e is the fundamental electronic charge, $E = \rho \times j$ is the electric field, ρ is the resistivity, j is the current density, Ω is the atomic volume, and $\frac{d\sigma}{dx}$ is the stress gradient along the line. Given the mass balance, the stress change in the interconnects can be derived as

$$\frac{\partial \sigma}{\partial t} = -\frac{d}{dx} \left[\frac{DB\Omega}{k_B T} \left(\frac{Z^* e E}{\Omega} - \frac{d\sigma}{dx} \right) \right], \quad (2)$$

where B is the effective bulk modulus of the nano-interconnect. The stress, σ , is the hydrostatic stress, thus the volumetric strain is connected to the stress through the effective bulk modulus. The interconnects were assumed to be initially void-free and voiding is assumed to be generated by the electromigration induced tensile stress once a critical stress is reached.

The void volume on the other hand is also calculated at each time increment based on the hydrostatic stress distribution,

$$Vol_{void}(t) = \left(\frac{1}{B} \right) \int_0^L (\sigma(x, t) - \sigma_0) dx, \quad (3)$$

where $\sigma(x, t)$ is the hydrostatic stress in copper, L is the length of the line and σ_0 is the initial stress.

Linewidth dependent calibration of the parameters required for the 1D Korhonen model (global module) and its implementation have been exhaustively described in our previous works^{16,18} which obviates the need for further elaboration here.

2. Local model

The calculation of void surface normal velocity is based on a continuum model of void/wire interface mass transport. The governing equations are

$$J_s = J_{st} + J_{sn}, \quad (4)$$

$$V_n = \left[-\frac{\partial J_{st}}{\partial s} + J_{sn} \right], \quad (5)$$

where J_{st} and J_{sn} are the atomic flux tangential to the void surface and normal to the void surface, respectively, and s is the arc length along the void surface.¹³

The tangential flux, J_{st} is given by the following expression:¹³

$$J_{st} = -\frac{D_s \delta_s}{K_B T} \left[e Z_s^* \rho j_t + \frac{\partial \mu}{\partial s} \right], \quad (6)$$

where D_s is the surface atomic diffusivity, δ_s is the void surface phase thickness, K_B is Boltzmann's constant, T is the temperature, e is the absolute electron charge, Z_s^* is surface effective charge number, ρ is the wire metal resistivity and j_t is the electron current density tangent to the void surface, μ is the atomic chemical potential on the void surface, which is given by¹³

$$\mu = \mu_0 + \Omega [E_{el} - \gamma k], \quad (7)$$

where μ_0 is a constant for reference chemical potential, γ is the surface free energy per unit area, k is the void surface curvature, and E_{el} is the elastic energy density. By substituting Eq. (7) into Eq. (6), J_{st} is derived as follows:

$$J_{st} = -\frac{D_s \delta_s}{K_B T} \left[e Z_s^* \rho j_t + \Omega \frac{\partial E_{el}}{\partial s} - \Omega \gamma \frac{\partial k}{\partial s} \right]. \quad (8)$$

Substituting from Eq. (8) into Eq. (5) the normal velocity, V_n is derived,

$$V_n = \frac{\delta_s}{K_B T} \frac{\partial}{\partial s} \left(D_s e Z_s^* \rho j_t + D_s \Omega \frac{\partial E_{el}}{\partial s} - D_s \Omega \gamma \frac{\partial k}{\partial s} \right) + J_{sn}. \quad (9)$$

From Eq. (9), four different velocity components are defined according to the underlying physical phenomena and the modeling approach,

$$V_n^{j_t} = \frac{\delta_s e Z_s^* \rho}{K_B T} \frac{\partial}{\partial s} (D_s j_t), \quad (10)$$

$$V_n^\gamma = -\frac{\delta_s \Omega \gamma}{K_B T} \frac{\partial}{\partial s} \left(D_s \frac{\partial k}{\partial s} \right), \quad (11)$$

$$V_n^{E_{el}} = \frac{\delta_s \Omega}{K_B T} \frac{\partial}{\partial s} \left(D_s \frac{\partial E_{el}}{\partial s} \right), \quad (12)$$

$$V_n^{Vol} = J_{sn}, \quad (13)$$

where $V_n^{j_t}$ corresponds to the velocity driven by current density tangent on the void surface, V_n^γ corresponds to velocity driven by surface tension, $V_n^{E_{el}}$ corresponds to the velocity driven by elastic stress on the void surface and V_n^{Vol} corresponds to the velocity driven by the normal flux of atoms exchanged between the void surface and the rest of the wire. In the modeling framework, $V_n^{j_t}$, V_n^γ and $V_n^{E_{el}}$ are resolved only over the void surface and as such, in the absence of the fourth component V_n^{Vol} , they can only lead to iso-volume morphology changes/migration. On the other hand, V_n^{Vol} dictates the volume changes of the void and is assumed to be equal to the net flux from the void which is calculated by the 1D Korhonen model which is solved over the entire interconnect in the global module. This is realised through fast diffusion paths (i.e., cap interface, grain boundaries) connected to the void surface which are explicitly modeled in the local module. From an implementation viewpoint, in order to ensure that the local module strictly follows the volume dictated by the global module at every increment and that the impact of the fast diffusion paths connected to the void surface on void morphology is captured, V_n^{Vol} is implemented as

$$V_n^{Vol} = C \times f(\theta), \quad (14)$$

where $f(\theta)$ is a normalized dimensionless function that takes into account the interaction of the void surface with the cap interface and grain boundaries, θ is the clockwise angle defined in a reference polar coordinate system that is employed to implement void kinetics with its origin placed on the void's centroid and C is a factor to be determined numerically by matching the void size with the size calculated by the global model. This implementation will be further justified in the next section on the impact of dimensional scaling and proven in [supplementary material](#).

In Eqs. (10)–(12), diffusivity is kept inside the differentiation operator given that it is considered a variable that depends on the location of the point of interest on the voids surface. Thereby, the impact of copper texture, i.e., anisotropic surface diffusivity of copper crystal and the impact of fast diffusion paths can be exhaustively addressed given that they result in variation of surface diffusivity over the void surface.

III. INTRINSIC IMPACT OF LENGTH SCALE ON VOID DYNAMICS

Starting from the equations of the void surface normal velocity components [Eqs. (10) and (11)], we reach a new formulation that can be generalized to all velocity components acting normal to the void surface which states that normal velocity can be defined as a product of: (i) a pre-factor which depends mainly on the physical parameters of the wire and void size and (ii) a normalized dimensionless polar function which takes values in the range from -1 to 1 and depends on the shape of the void regardless of its size. Hence, the normal velocity of the void surface is expressed by the expression (complete derivation for all this section is in

supplementary materials, Sec. 1),

Velocity normal to void surface(θ) = prefactor with the unit of velocity
 × Dimensionless normalized function (θ).

Assuming that the current density far from a void in a wire is, j_{wire} , then the void surface normal velocity under the impact of current density's tangent on void surface can be analytically derived as follows:

$$V_n^j = \left[\frac{D_s \delta_s e Z_s^* \rho_j^{wire} \times F_{j_i, max}}{K_B T \times r_{mean}} \right] \times F_{j_i, norm}(\theta), \quad (15)$$

where $F_{j_i, norm}(\theta)$ is a dimensionless function which can take values between -1 and 1 . $F_{j_i, max}$ is a dimensionless parameter coming from normalization of void shape function (see supplementary material) and r_{mean} is the average radius of the void. Similarly, for the void surface velocity under the impact of surface energy it can be shown that

$$V_n^\gamma = - \left[\frac{D_s \delta_s \Omega \gamma \times F_{\gamma, max}}{K_B T \times r_{mean}^3} \right] \times F_{\gamma, norm}(\theta), \quad (16)$$

where $F_{\gamma, norm}(\theta)$, is a dimensionless function which can take value between -1 and 1 , where $F_{\gamma, max}$ is a dimensionless parameter coming from normalization of void shape function (see supplementary material). Thereby, the ratio of $\left| \frac{V_n^\gamma}{V_n^j} \right|$, will take a value <1 if the impact of void surface current density is dominant and, conversely, it will acquire a value >1 if the impact of void surface energy is dominant,

$$\left| \frac{V_n^\gamma}{V_n^j} \right| = \frac{\Omega \gamma \times F_{\gamma, max}}{e Z_s^* \rho_j^{wire} \times F_{j_i, max} \times r_{mean}^2}. \quad (17)$$

Hereby, a critical mean void radius, r_{crit} , can be defined as the radius for which $|V_n^\gamma| = |V_n^j|$,

$$r_{crit} = \sqrt{\frac{\Omega \gamma \times F_{\gamma, max}}{e Z_s^* \rho_j^{wire} \times F_{j_i, max}}}. \quad (18)$$

Although the absolute values of, $F_{\gamma, max}$ and $F_{j_i, max}$, can only be calculated numerically as they depend on void shape, using (17) and (18) the competition between the impact of electromigration on void surface and the impact of surface energy can be deciphered, where as shown in Fig. 1, for voids smaller than r_{crit} the surface energy has a dominant role. Of note, electromigration effects favor slit morphology formation whereas surface energy induces circular morphology.¹¹⁻¹³

IV. NUMERICAL IMPLEMENTATION OF VOID EVOLUTION AT THE LOCAL LEVEL

The central part of the simulation based on the models presented in the previous sections is calculation of the normal velocity of the void surface. For each time step of the discretized simulation

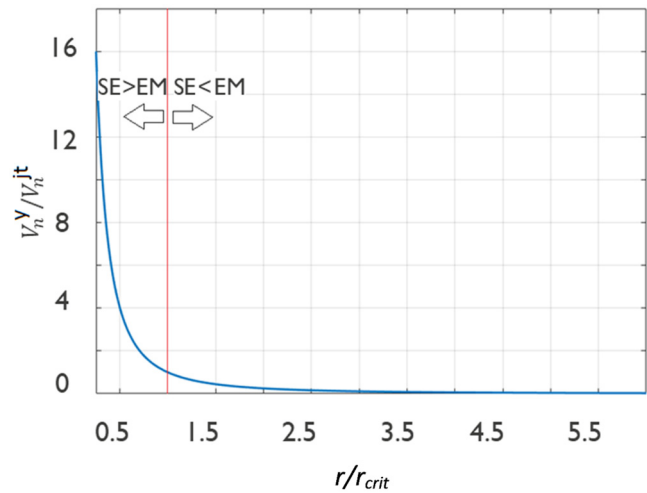


FIG. 1. Competition between surface energy (SE) and electromigration (EM) in terms of void morphology evolution as a function of void length-scale.

time, the normal velocity for each point at the void surface is calculated and applied for the spatial movement of the point on the 2D domain. The movement of all points at the void surface leads to the change of the void shape. In the subsequent time steps, the procedure is repeated, i.e., the normal velocity is calculated for the newly determined void shape and used for the shape transformation until the predefined simulation time is reached. The 2D local model domain is defined as the midplane across the line and via, see Fig. 2.

The void boundary is defined using a polar function $r(\theta)$ and the origin of the polar coordinate system coincides with the void's centroid with a location variable, Loc , see Fig. 2.

At every increment of the simulation (i) a diffusivity calculation module determines the surface diffusivity of every location on the void boundary depending on the microstructural details which are provided as input (ii) a velocity calculation module determine the velocity of every point on the void boundary based on Eq. (9), (iii) void boundary module resolves the void boundary at the

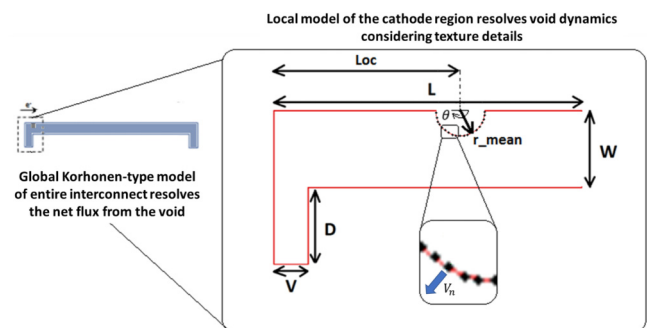


FIG. 2. Schematic of the modeling framework.

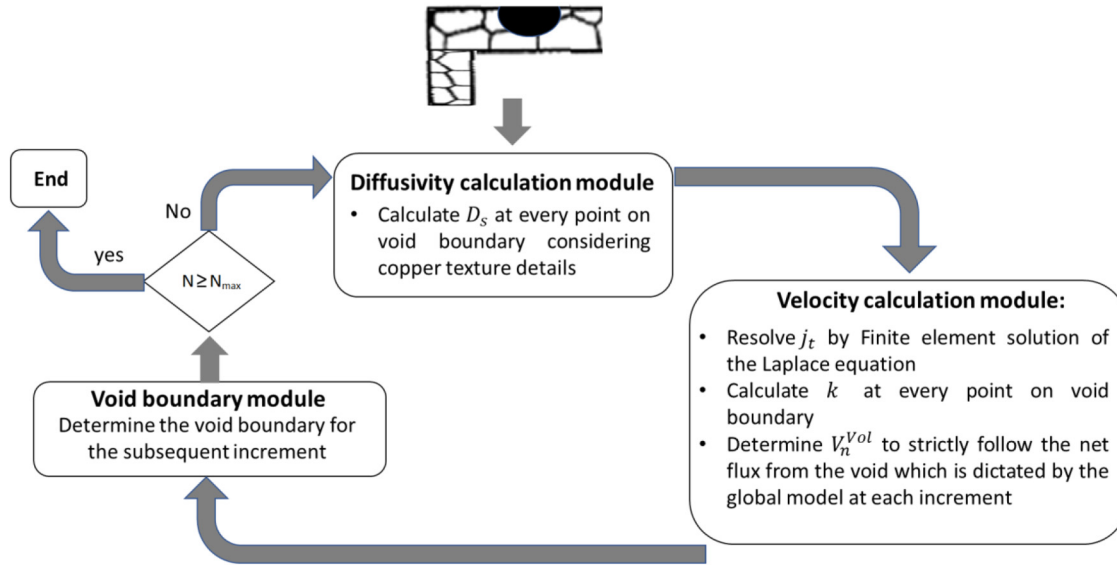


FIG. 3. The flow chart of operations conducted in the modular structure of the local model, where N is the number of iterations.

subsequent increment given the calculated void boundary normal velocities, see Fig. 3. The details of each module are provided as follows:

A. Diffusivity calculation module

The modeling of the diffusivity distribution in the local domain of the modeling framework is of central importance, since it defines an interaction between void and copper microstructure. Rather than setting a single effective value for diffusivity which obscures the impact of local microstructural features on the void evolution, we model diffusivity as a distributed parameter which is a function of spatial coordinates. On the void surface itself, the local diffusivity is a function of the angle θ . This local surface diffusivity may widely vary along the void boundary given that it may cross several grains, each with a distinct orientation. In this context, it has been shown that for the FCC copper lattice, D_{s111} is larger than D_{s100} and D_{s110} by 4 and 6 orders of magnitude, respectively, at 150 °C.¹⁹

As such, in order to implement this paradigm, in the initial step of the simulation, for an input local microstructure, appropriate diffusivity values are assigned in the 2D local domain. For modeling of the anisotropic diffusivity at the surface of the evolving void in the FCC crystal we rely on the previous works.^{11,20,21} According to these works, surface diffusivity is defined by a three-parameter function

$$D_s(\theta, T) = D_0(T) \times (1 + m[1 - \cos(n\theta_{tan} - \theta_0)]), \quad (19)$$

where

$$D_0(T) = D_{s0} \exp\left(-\frac{E_a}{kT}\right),$$

where D_{s0} is the exponential pre-factor of atomic diffusivity of material, E_a is the activation energy, θ_{tan} is the angle between the tangent to the void surface and longitudinal axis, m is the degree of anisotropy with $m = 0$ corresponding to the isotropic case, n is the crystallographic symmetry, θ_0 is the orientation of the interconnect line with respect to FCC crystal planes. While the value of interfacial diffusivities, i.e., along grain boundaries and Cu/Cap interface can be readily employed from the existing literature, the value of diffusivity across grain boundaries is not obvious. The latter needs to be determined when the void surface crosses the grain boundaries. This is resolved by allocating a thickness to grain boundaries and fitting a Piecewise Cubic Hermite Interpolating Polynomial (PCHIP) function in Matlab®, where the value of surface diffusivity is known in the two adjacent grain surfaces and the fitting function provides a smooth differentiable diffusivity function across the grain boundary. At the start of simulation, the diffusivity values along the interfaces between each two sub-domains are still unknown. These diffusivity values are estimated only when the evolving void surface starts to intersect the interface. They are estimated using a PCHIP fit based on the known points giving a smooth differentiable diffusivity function in terms of the void's polar angle.

B. Velocity calculation module

In this module, the four components of void normal velocity described by Eqs. (10)–(13) are calculated by submodules and the total surface normal velocity is obtained. The first sub-module is a

PDE solver that solves Laplace differential equation and determines the current density around the void surface using finite element modeling (FEM), where second order 6-node triangular elements were employed for meshing and the mesh size was determined by a sensitivity analysis to ensure that a stable solution is reached that is no longer sensitive to mesh refinement. The second sub-module calculates the curvature from the polar function describing the void surface $r(\theta)$ using the following equation:²²

$$\kappa(\theta) = \frac{|r^2 + 2(r')^2 - rr''|}{(r^2 + (r')^2)^{\frac{3}{2}}}, \quad (20)$$

where $\kappa(\theta)$ is the local curvature as a function in θ .

The third sub-module determines the strain energy distribution over the void surface from an input stress map and the fourth sub-module calculates the normal velocity component which rises due to the normal vacancy flux to the void surface determined by the global Korhonen-type model. As described in Eq. (14) and elaborated in the [supplementary materials](#) Sec. 1, every surface velocity component can be described by the product of a pre-factor which depends on physical parameters and a normalized dimensionless function, which only depends on the void shape and the diffusivity paths it crosses. As such, the normalized function for void growth is obtained by normalizing the local surface atomic diffusivity in the direction normal to the void surface. Subsequently the pre-factor is determined using numerical iterations until the void size change follows the volume dictated by the global model.

4.3. Void boundary module

At each iteration, the surface points are allowed to move, as a maximum limit, a predefined distance of approximately 0.017 of r_{mean} (small fraction of r_{mean} obtained by sensitivity studies). The time for each step is determined as the quotient of this predefined maximum distance by the maximum calculated normal surface velocity from all points on the void boundary. Finally, each point travels a distance equal to the product of this estimated time and its own normal velocity. This procedure gives a dynamic time step for each iteration and ensures that at each iteration each point's displacement is small enough so as the assumption of constant velocity over this displacement remains valid.

V. RESULTS AND DISCUSSION

In this section, six case studies are presented in order of complexity. In all these cases the local simulation domain consists of the cathode area of a copper dual damascene interconnect including the cathode via and the adjacent segment of the line where the interconnect is operating under an upstream electromigration mode with larger cross-sectional area of the line compared to the via assuming line's aspect ratio to be 2. In [Tables I](#) and [II](#) we describe all used parameters used in the case studies.

What is left to mention here is the description of the case control parameters which have unique values for each case. S is the geometrical scaling factor (applied as shown in [Table I](#)), Loc is the initial void position along the interconnect (see [Fig. 2](#)), j_{wire} is the operational current density in the line far from void and via, $\frac{d\sigma}{dx}$

TABLE I. The geometrical parameters of the void dynamics simulation domain as determined in [Fig. 2](#) in addition to H as the thickness of the wire in the direction normal to the simulated cross section, S as the geometrical scaling factor, and r_0 as the initial mean radius of the void.

Parameter	Value	Unit
W	$S \times 44$	nm
L	$S \times 176$	nm
D	$S \times 44$	nm
V	$S \times 22$	nm
H	$S \times 22$	nm
r_0	$S \times 20$	nm

is the stress gradient acting along the line which is applied as an initial condition, m , n and θ_0 as described before in Eq. (19).

A. Case study 1: Iso-volume (transport only tangent to void surface), void evolution considering transport over void surface by electric current assuming homogeneous isotropic domain

For this case, the input parameters were assumed to be $Loc = 0.5L$, $j_{wire} = 5 \times 10^{10}$ A/m², $\frac{d\sigma}{dx} = \frac{d\sigma}{dy} = 0$, isotropic diffusivity [i.e., $m = 0$ in Eq. (19) and $T = 100^\circ\text{C}$]. Considering $S = 1$. The simulations determine that $r_{critical}$, as described by Eq. (18), lies between 62 and 80 nm at different stages of void evolution. Given that $r_0 < r_{critical}$, surface tension is much stronger than the electromigration component causing a very fast transformation of an elliptical void to a circular void, [Fig. 4\(a\)](#). During this transformation, the surface tension drops to almost zero and the electromigration starts to drive the nearly circular void toward the cathode end. As the void transforms quickly into a circle, the interconnect's local resistance also drops quickly, [Fig. 4\(b\)](#). The shape transformation toward a circular void also reduced the current crowding effect and thus weakens electromigration-component at the void surface leading to a lower migration velocity of the void, [Fig. 4\(c\)](#).

TABLE II. Wire material physical parameters based on copper metallization.

Parameter	Description	Value	Unit	Reference
E_{eff}	Effective Bulk modulus	12	GPa	23
ν	Poisson ratio	0.3		23
ρ	Resistivity	50	$\Omega \text{ nm}$	16
γ	Surface free energy	1	J/m ²	24
T	Temperature	100	C	...
Z^*	Free surf. effective charge number	30		2
D_s	Void free surface diffusivity	1×10^{-12}	cm ² /s	25
D_g	Grain boundary diffusivity	3×10^{-15}	cm ² /s	25
D_C	Cap surface diffusivity	4×10^{-16}	cm ² /s	2

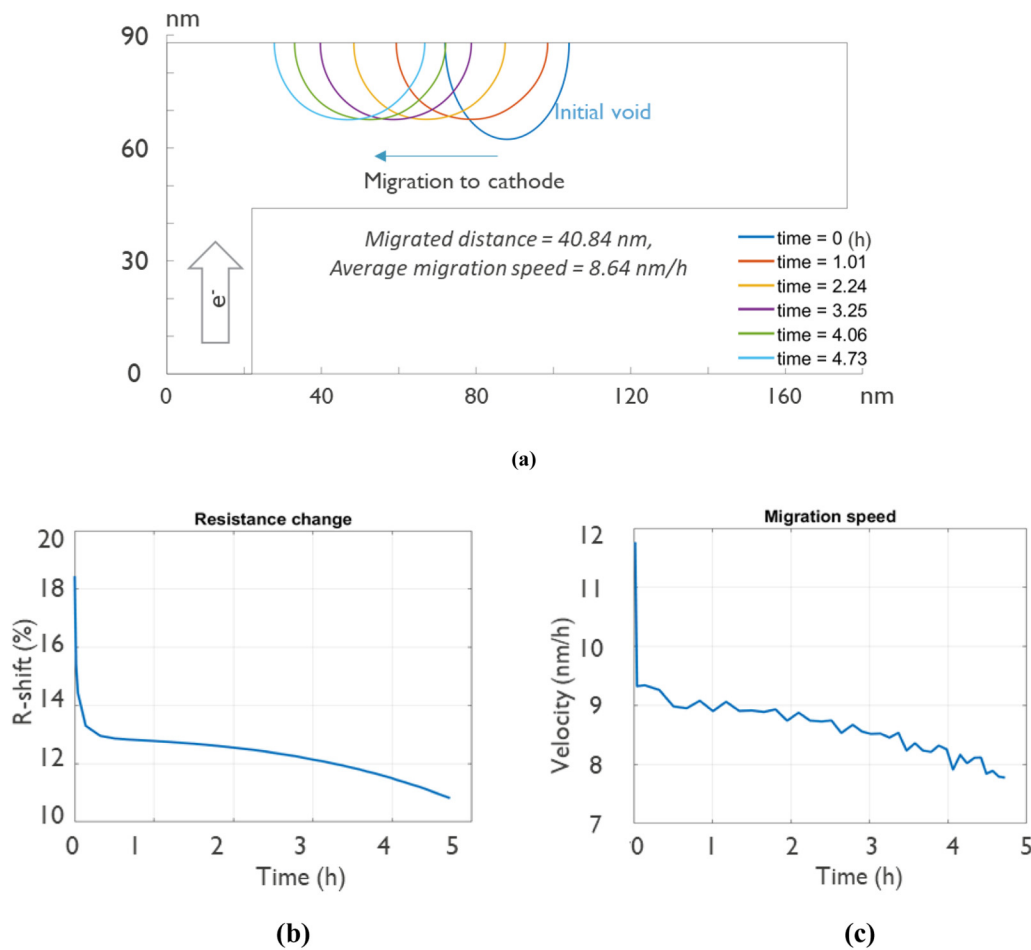


FIG. 4. The simulation results for case study 1 applied to narrow interconnects (see video “Case 1.1.avi” of the [supplementary material](#)), (a) void evolution (b) local resistance shift and (c) void migration velocity as a function of time.

To shed light on the impact of dimensional scaling of interconnects, in another simulation, the scaling factor was assigned to be $s = 13$ where all other parameters including j_{wire} were kept unchanged. This scaled the wire thickness to 572 nm and void mean radius to 260 nm, which resulted in a regime where $r_0 > r_{critical}$. The electromigration component is stronger than surface tension causing a transformation of an elliptical void to a wedge-shaped void, [Fig. 5\(a\)](#). Moreover, as the void approaches the via, the change of current direction and current crowding at the via-line conjunction led to an unbalanced current density around the void which generated a slit morphology. Both the electromigration as well as the surface energy induced velocities, decrease for larger dimensions, as explained by Eqs. (15) and (16). There is a relatively fast drop of resistance as the elliptical void transforms and interrupts a smaller cross-sectional area of the line, followed by a slower decrease during void’s further migration toward the end of the line. Given that no void growth was assumed, void migration to the end of the line, where there is effectively no current due to via-line conjunction

current crowding, minimized the resistance shift, see [Fig. 5\(b\)](#). Similarly, there is a relatively fast reduction of migration velocity following transformation of the elliptical void to a wedge shape, see [Fig. 5\(c\)](#).

As such, dimensional down-scaling by 13 folds resulted in approximately 10-fold increase of void’s migration velocity under identical operational current density and temperature. One practical implication of this finding is that cross-sectional scaling of copper dual damascene interconnects enhances via-failure modes as voids promptly migrate toward the via and continue further growth resulting to early failures.

B. Case study 2: Iso-volume void evolution considering transport over void surface by a stress gradient assuming homogeneous isotropic domain

The impact of void’s position in the applied stress field and the effect of scaling were investigated. The interaction of the void

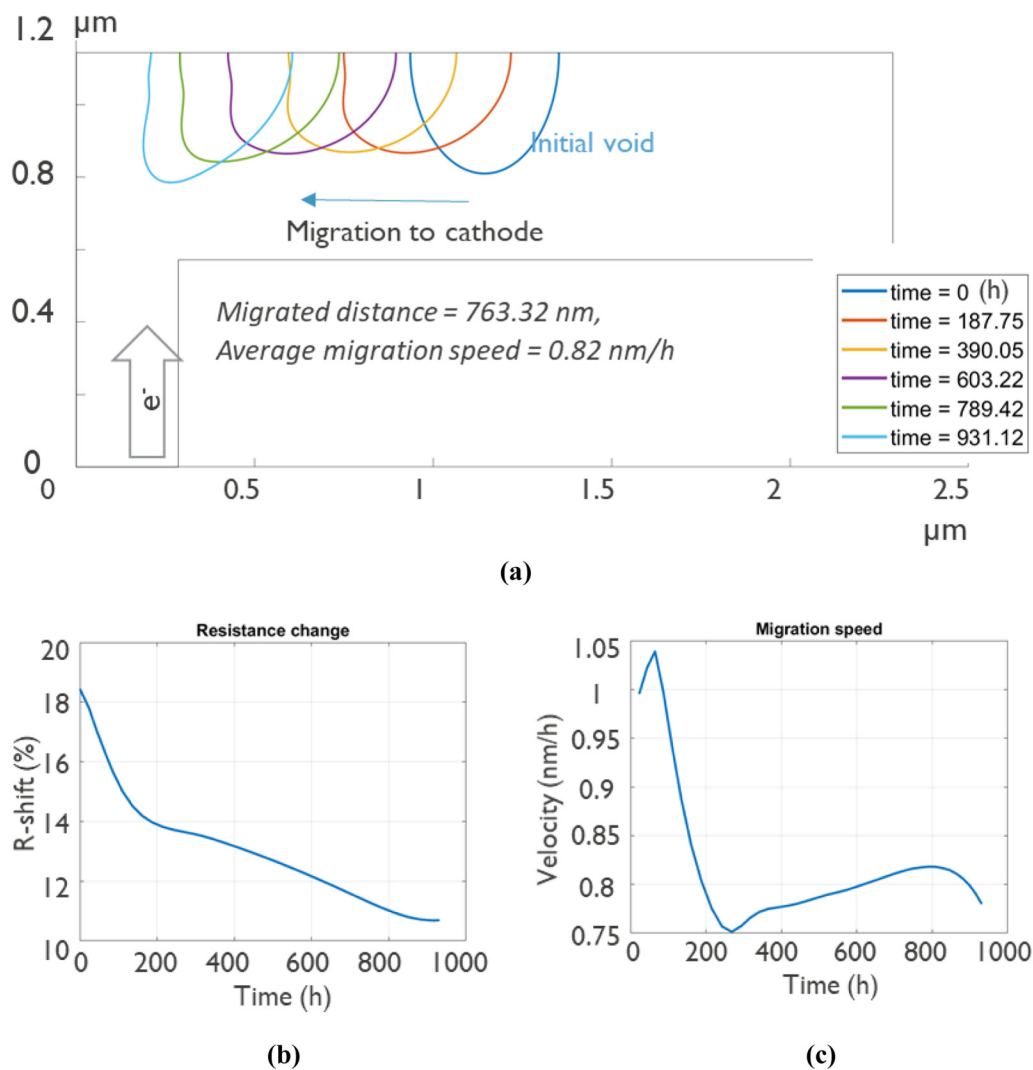


FIG. 5. The simulation results for case study 1 applied to wide interconnects (see video “Case 1.2.avi” of the supplementary material), (a) void evolution (b) local resistance shift and (c) void migration velocity as a function of time.

with a stress gradient along the line in the absence of any electrical current is shown in Fig. 6. Figure 6(a) shows the considered distribution of hydrostatic stress along the line mostly caused by vacancy redistribution, and the response of the void to the stress gradient is shown in Figs. 6(b), 6(c) and 6(d). For this case, the input parameters were assumed to be: $Loc = 0.5 L + Sr_0$ in case the void is in the compressive side or $Loc = 0.5 L - Sr_0$ in case the void is in the tensile side, $j_{wire} = 0$, $\frac{d\sigma}{dx} = 1 \text{ MPa/nm}$, $\frac{d\sigma}{dy} = 0$, isotropic diffusivity [$m = 0$ in Eq. (19)] and $T = 100 \text{ }^\circ\text{C}$. In Fig 6(b), the line thickness is only 44 nm and the void is initially located toward the tensile half of the line. In Figs. 6(c) and 6(d), the line has a thickness up-scaled to 572 nm with the initial void positioned at the tensile and compressive sides, respectively. The simulations show that the void maintains more of a circular morphology at a lower length scale

due to significance of surface energy driven surface velocity [Fig. 6(b)], whereas, at the larger length-scale a longitudinal extension of the void is evident, i.e., the void stretches along the stress gradient [Figs. 6(c) and 6(d)]. The void migrates toward higher magnitude of stress irrespective of the stress sign (i.e., compressive or tensile) given that the surface velocity is related to the strain energy density [Eq. (12)] which is independent from stress sign as follows:

$$E_{el} = \frac{\sigma_{hyd}^2}{2B}, \quad (21)$$

where σ_{hyd} is the hydrostatic stress and B is the effective bulk modulus of the interconnect. Nevertheless from Figs. 6(c) and 6(d),

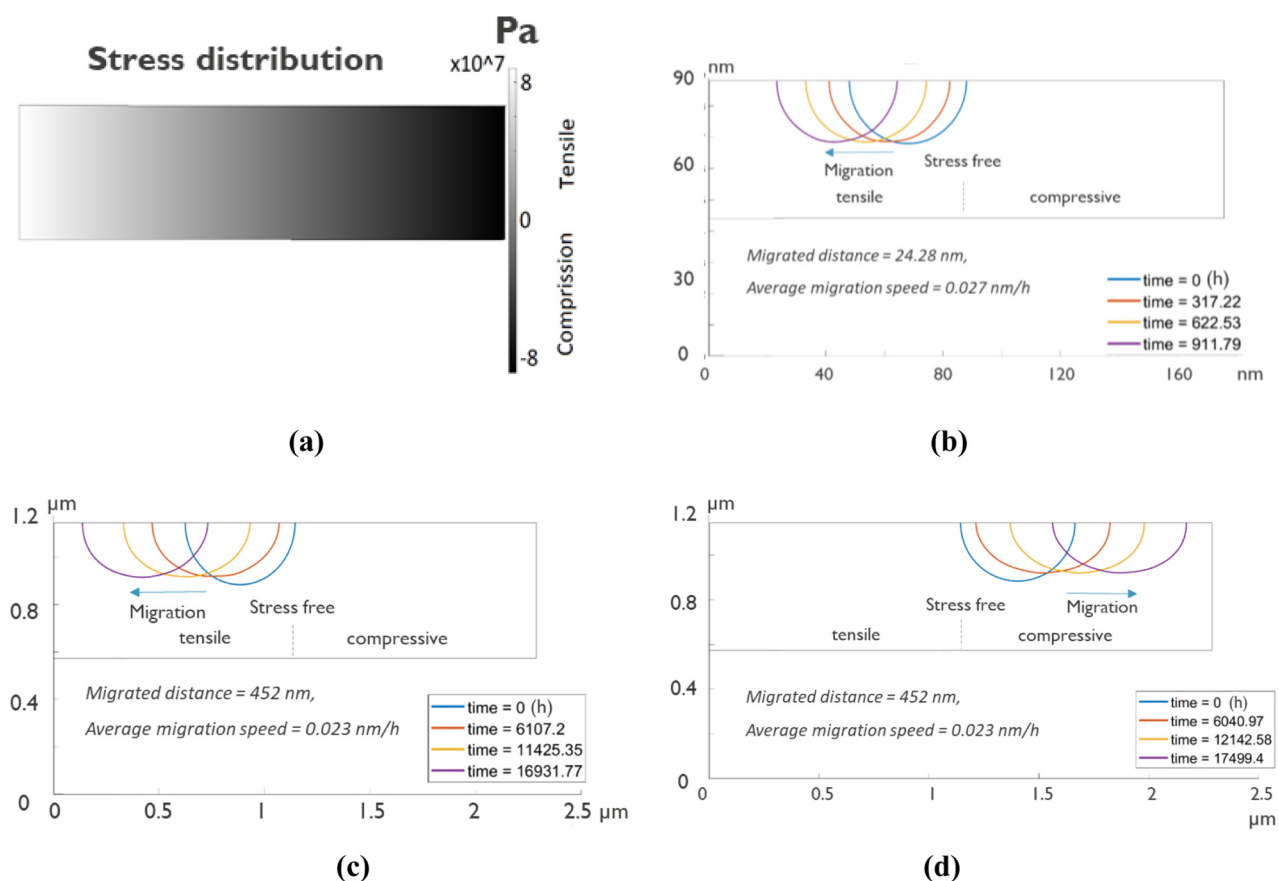


FIG. 6. Void dynamics in response to a hydrostatic stress gradient along the interconnect assuming iso-volume transformations (a) the considered input stress distribution along the line (b) response of a cylindrical void in a 44 nm thick interconnect initially located at the tensile side (c) response of a cylindrical void in a 572 nm thick interconnect initially located at the tensile side (d) response of a cylindrical void in a 572 nm thick interconnect initially located at the compressive side (see video “Case 2.1.avi” of the [supplementary material](#)).

it is obvious that the initial position of the void determines whether it moves up or down the stress gradient. If the void is initially in the compressive side, it will continue migrating toward higher magnitudes of compressive stress and if it is initially at the tensile side it will migrate toward higher magnitudes of tensile stress. Such behavior is consistent with the previous findings in Ref. 26.

Figures 7(a) and 7(b) demonstrate the migration velocity under the impact of the longitudinal stress gradient in the absence of any electrical current for a 44 nm thick and 572 nm thick line, respectively. Clearly for a given stress gradient, the migration velocity is independent of the length scale. Moreover, a zero migration velocity exists when the center of the void lies exactly at the stress free point with a continuous acceleration of migration as the void gets away from this point. These results are further explained and proven analytically in [supplementary materials](#), Sec. 2.

On the other hand, a stress gradient across the line thickness causes the void to deform across the interconnect which favors a slit morphology with larger impact on resistance shift, see Fig. 8. The considered stress gradient magnitude is chosen to be consistent with the

range of process-induced thermomechanical stresses in nano-interconnects.²⁷ The intensity of such slit-like morphology depends again on the wire dimensions, where, the impact is more significant for thicker dimensions given a weaker counter-effect from the surface energy induced velocity which favors circular morphology in order to minimize the Laplacian of void surface curvature.

Previous published studies suggest that, in terms of void surface velocity, the contribution from current density component and surface energy components are dominant over the strain energy density component. For example, Rice and Chuang showed that, in most cases, the contribution due to surface energy greatly exceeds the strain energy term.²⁸ Castro *et al.* demonstrated that their void velocity calculations neglecting the strain energy density component can accurately predict experimental results.²⁹ These findings are consistent with our findings, where, by comparing void kinetics, e.g., the time taken for the void to migrate same distance in case 5.1 and case 5.2 for the same length scale, the dominance of current density component over the strain energy density component can be clearly appreciated.

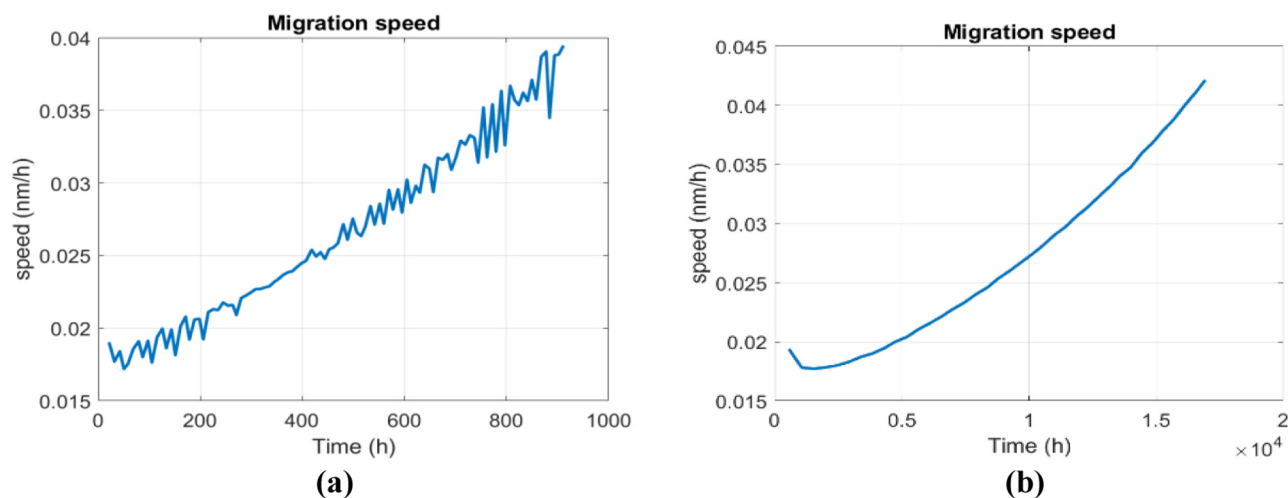


FIG. 7. Migration velocity under a longitudinal stress gradient along the line (a) for a 44 nm thick line and (b) for a 572 nm thick line.

C. Case study 3: Iso-volume void evolution considering transport over void surface by electric current assuming heterogeneous isotropic domain

In this case, we evaluate the voids response if it evolved through two isotropic regions with different diffusivities. In practice, regions of different effective diffusivity exist in an interconnect, e.g., polycrystalline vs. bamboo segments along an interconnect,² which put this case study into context. First assuming it starts in high diffusivity region and evolves into a low-diffusivity region and also a different scenario where it starts in a low-diffusivity region and evolves into a high-diffusivity region. The input parameters are assumed to be $Loc = 0.5 L$, $j_{wire} = 5 \times 10^{10} \text{ A/m}^2$, $\frac{d\sigma}{dx} = \frac{d\sigma}{dy} = 0$, isotropic diffusivity [i.e., $m = 0$ in Eq. (19)], $S = 13$ and $T = 100^\circ\text{C}$. Shape transformations are iso-volume given that transport is considered to occur only on the void surface. It is assumed that the diffusivity changes by 6 folds between the two regions with the lower diffusivity value of

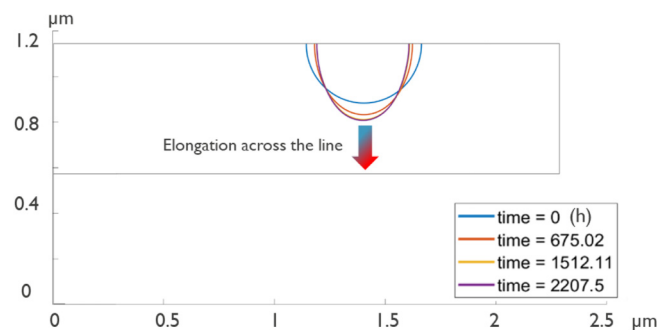


FIG. 8. Morphological transformation of a void under the influence of the stress gradient of $\frac{d\sigma}{dy} = 2 \text{ MPa/nm}$ and $\frac{d\sigma}{dx} = 0$ across the line thickness (see video "Case 2.2.avi" of the [supplementary material](#)).

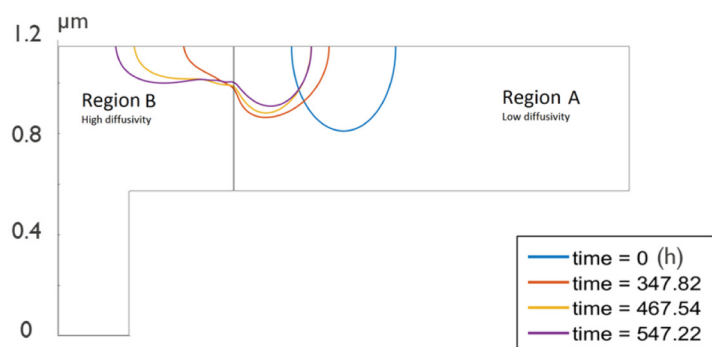
$10^{-12} \text{ cm}^2/\text{s}$.²⁵ Interestingly only a 6-fold difference in diffusivity results in drastic void shape variations.

In Figs. 9(a) and 9(b), the longitudinal elongation of an initially elliptical void migrating into a region with higher effective diffusivity and the resulting drop of resistance induced by the void are shown, respectively. Inverting the two regions will result in a scenario where the void elongates across the two region's interface and causes an increase in the local electrical resistance. The latter occurs relatively faster given that the void is initially in the region with a higher diffusivity which expedites the kinetics [see Figs. 9(c) and 9(d)]. In addition, a drop of void's longitudinal migration velocity (i.e., void pinning by the low diffusivity region) is clearly demonstrated in Fig. 9(f).

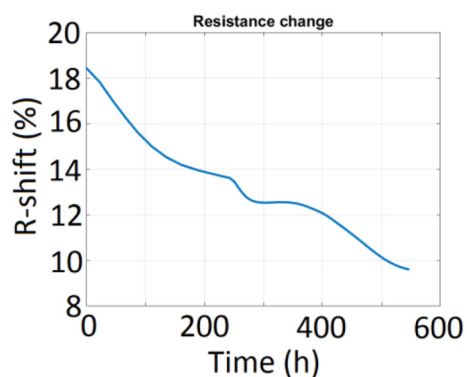
D. Case study 4: Iso-volume void evolution considering transport over void surface by electric current considering a homogeneous domain with anisotropic diffusivity of copper's FCC lattice

In this case study, the void is considered to reside in a single copper grain in the line adjacent to the cap interface, while the strong anisotropic nature of diffusivity in the copper's FCC lattice is considered. The transport is considered to only occur on the void surface (i.e., iso-volume transformation) in response to electric current only. Due to anisotropic diffusivity, at every location along the void boundary, diffusivity is a function of the angle, θ .

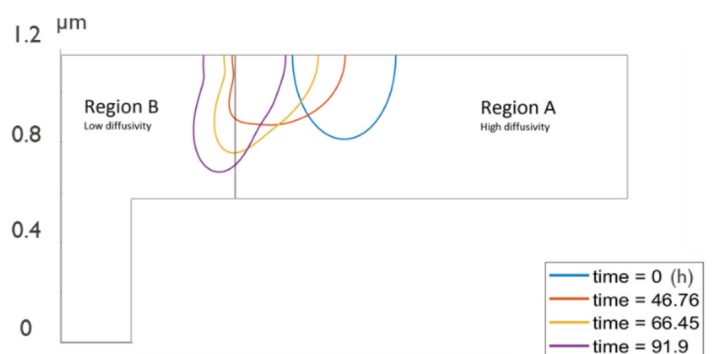
First, the simulations were conducted with the following input parameters: $Loc = 0.5 L$, $j_{wire} = 5 \text{ MA/cm}^2$, $\frac{d\sigma}{dx} = \frac{d\sigma}{dy} = 0$, $T = 100^\circ\text{C}$, considering $S = 13$, and anisotropic diffusivity [i.e., $\theta_0 = \pi$, $m = 50$, $n = 4$ in Eq. (19)]. The latter results in a diffusivity variation over the void surface ranging from 2×10^{-14} to $2 \times 10^{-16} \text{ m}^2/\text{s}$ on the 100 and 110 planes, respectively, as demonstrated in Fig. 10(a). In stark contrast to the case assuming isotropic diffusivity, considering the anisotropy of the FCC Cu lattice results in a faceted morphology, see Fig. 10(b).



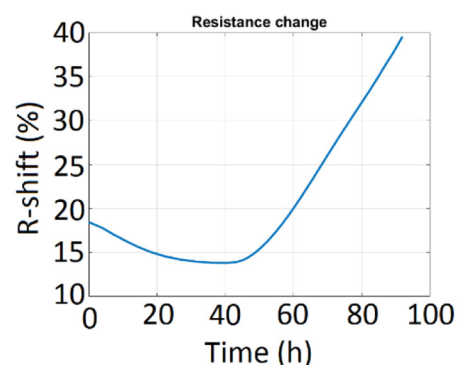
(a)



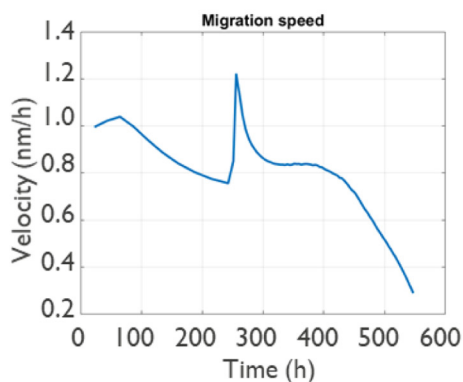
(b)



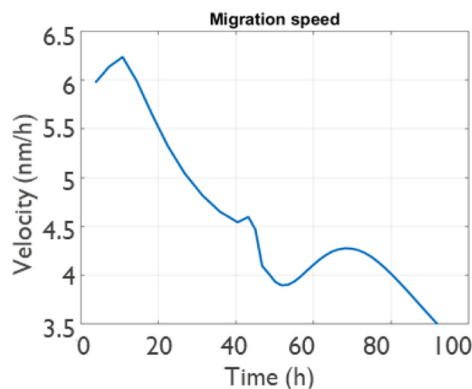
(c)



(d)



(e)



(f)

FIG. 9. Morphological transformation of an iso-volume void through isotropic regions of different diffusivity, its impact on local resistance shift, and longitudinal migration velocity of the void's centroid (a), (b), and (e): from migration from low to high diffusivity regions (c), (d), and (f): from high to low diffusivity regions (see videos "Case 3.1.avi" and "Case 3.2.avi" of the [supplementary material](#)).

In order to better understand the impact of crystal orientation, the FCC lattice was rotated by 45° , [i.e., $\theta_0 = 0$, $m = 50$, $n = 4$ in Eq. (19)] [Fig 11(a)]. Interestingly, this lattice rotation resulted in a 40% increase of average migration speed of the void's centroid.

In addition, as shown in Fig 11(b), the void morphology upon transformation has a larger resistive impact given that the void occupies a larger cross-sectional area of the line as compared to $\theta_0 = \pi$. In addition, an over-shoot of resistance and velocity

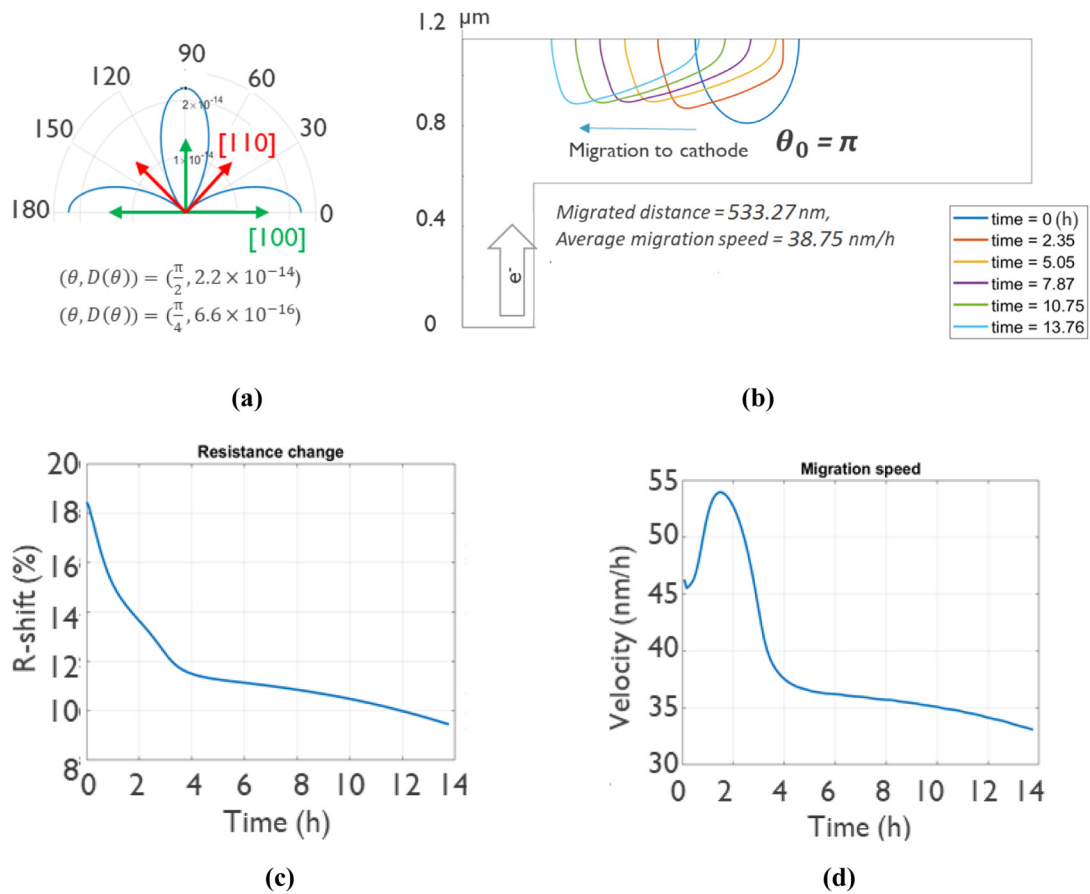


FIG. 10. (a) Polar plot of diffusivity variation over the void surface, vectors demonstrate FCC crystal plane normals (b) void evolution (see video "Case 4.1.avi" of the supplementary material) (c) local resistance shift and (d) void migration velocity as a function of time.

occurred at $t \sim 12$ h, which is due to a strong slitting of the void across the line [Figs. 11(c) and 11(d)]. This morphology translation can be explained by the current vector re-orientation and crowding at the via-line conjunction as shown in Fig. 12.

In both cases, as the void gets closer to the via-line conjunction, the current crowding effect causes the void to elongate along one of the directions with a high diffusivity value, however in the case where $\theta_0 = \pi$ this elongation causes the void to block less current causing a drop in resistance shift [see Fig. 10(c)] while in the case where $\theta_0 = 0$ this elongation favors more a slit shape that blocks more of the current causing the increase in resistance [see Fig. 11(c)].

E. Case-study 5: Void interaction with a grain boundary; iso-volume void evolution considering transport over void surface by electric current in a heterogeneous domain with anisotropic diffusivity of copper's FCC lattice

In this case study, the local domain consists of two copper grains with distinct orientation considering the anisotropic diffusivity of the FCC copper lattice in each grain. The void initially

resides within one grain, and under the influence of electrical current, it migrates through the grain boundary into the adjacent grain. Similarly, here the transport is considered to occur only on the void surface under the influence of electrical current and therefore the void preserves its volume. As such, the grain boundary is realistically represented by the fact that it delineates the boundary between the two copper crystals with distinct orientations. To this end, the input parameters considered in the simulation are as follows: $Loc = 0.65 L$, $j_{wire} = 5 \text{ MA/cm}^2$, $\frac{d\sigma}{dx} = \frac{d\sigma}{dy} = 0$, $T = 100 \text{ }^\circ\text{C}$, considering $S = 13$, and anisotropic diffusivity where the orientation of the two grains changes by 45° (i.e., $m = 50$, $n = 4$, $\theta_0^{grain A} = 0$, and $\theta_0^{grain B} = \pi$). The latter results in a diffusivity variation over the void surface as demonstrated in Fig. 13(a), for a void migrating through the grain boundary.

As demonstrated in Fig. 13(b). when the void is fully in each separate grain, it adopts the shape corresponding to the specific orientation of that grain as shown in Figs. 10(b) and 11(b). However, during migration through the grain boundary, adjacent to the grain boundary a high gradient of diffusivity exists causing a high

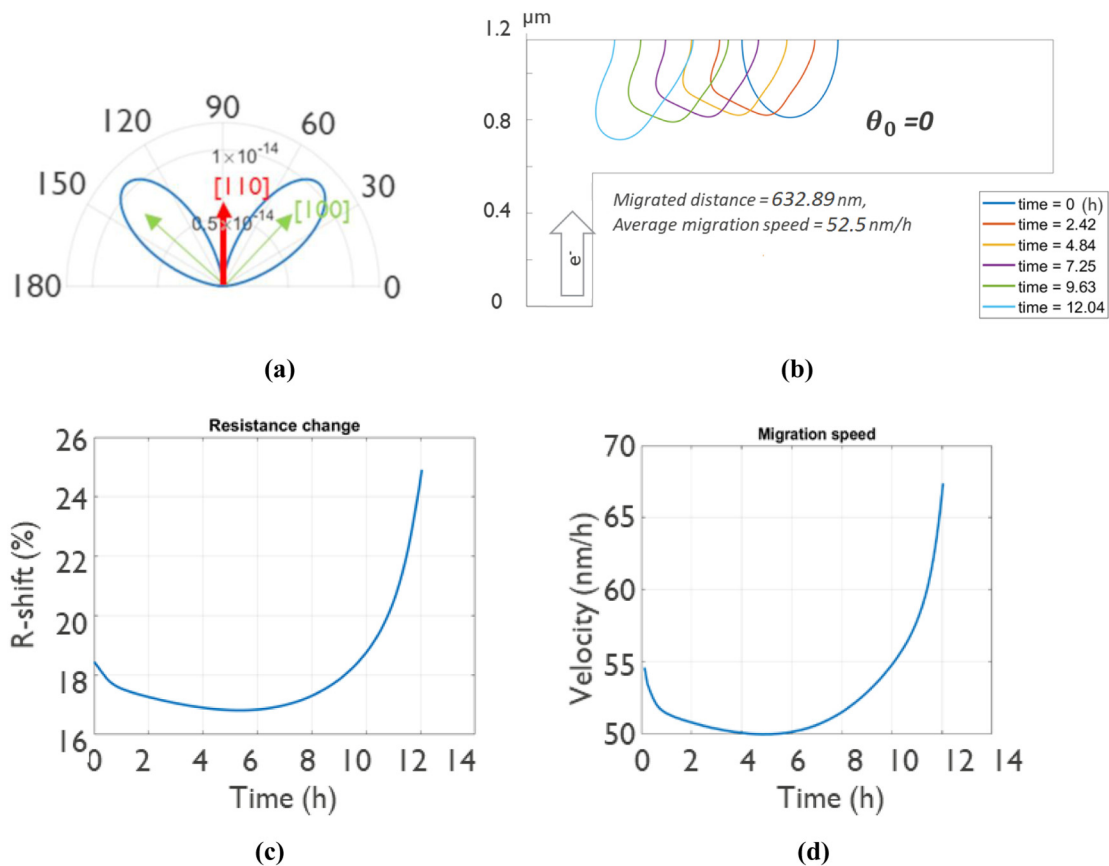


FIG. 11. (a) Polar plot of diffusivity variation over the void surface, vectors demonstrate FCC crystal plane normals (b) void evolution (see video “Case 4.2.avi” of the supplementary material) (c) local resistance shift and (d) void migration velocity as a function of time.

tangential flux divergence, which leads to high normal void surface velocity and an extension of the void along the grain boundary, see Fig. 13(b). This was realized given a smooth differentiable diffusivity function across the grain boundary as discussed in Sec. IV A. As



FIG. 12. (a) Current density distribution map in the cathode area shown strong crowding at the via-line conjunction.

demonstrated in Figs. 13(c) and 13(d), the void interaction with grain boundary causes an abrupt increase in both R-shift and migration speed during transition through the grains.

F. Case-study 6: Void growth and impact of fast diffusion paths (i.e., along grain boundary and cap interface) on growth patterns

In this case study, the void volume evolution is determined using the global model described in Sec. II A. 1. The electromigration induced volume increase is calculated for a 44 nm thick and 100 μm long copper interconnect with cobalt cap under a current density of $j_{\text{wire}} = 1 \text{ MA/cm}^2$, $\frac{d\sigma}{dx} = \frac{d\sigma}{dy} = 0$, $T = 100^\circ\text{C}$ and the void volume is dictated to the local model (i.e., void dynamics module) at every time increment. Initial void position is $Loc = 0.6 L$. The calibration approach and the effective properties used in the global model of the interconnect are described in detail in Refs. 16 and 18.

The local model is employed to predict different void morphologies for the growing void depending on the contribution of the local fast diffusion paths, which transport ion from the void to the entire wire. Figure 14(a) shows the void size evolution with time as determined by the global model. In Fig. 14(b), the void

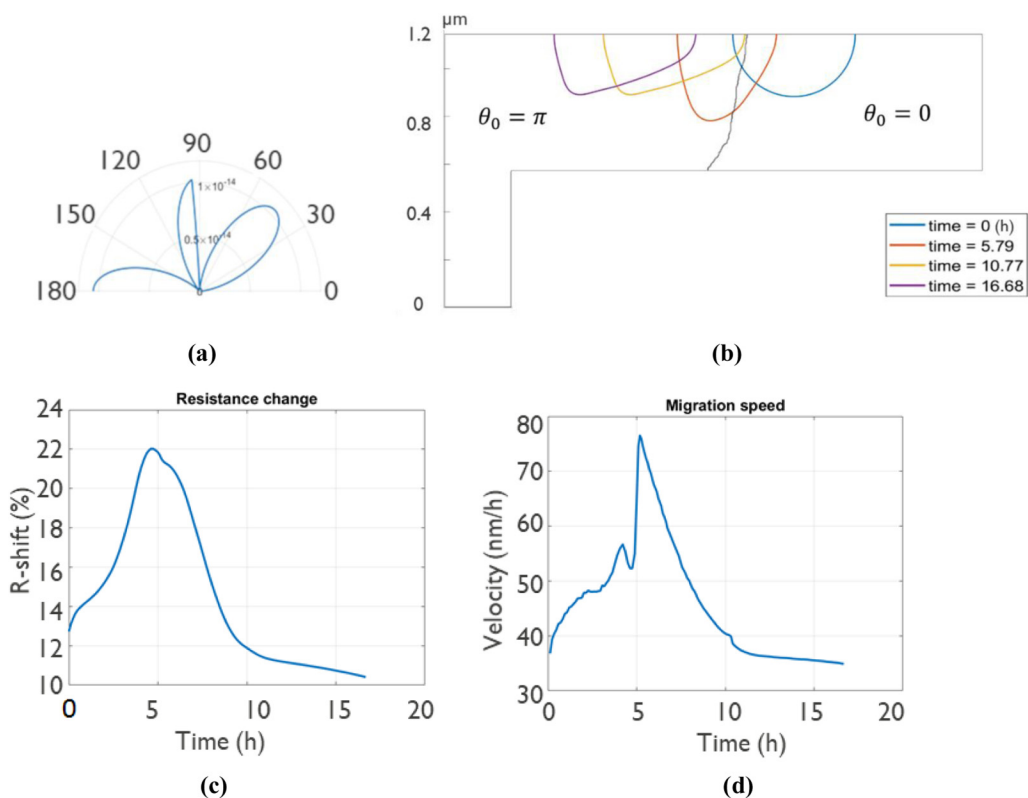


FIG. 13. (a) Polar plot of diffusivity variation over the void surface when the void is passing through the grain boundary when the grain boundary cuts the void surface at angle of 90° (b) void evolution (see video “Case 5.avi” of the [supplementary material](#)) (c) local resistance shift and (d) void migration velocity as a function of time.

growth pattern at the local level is simulated for a case where all the outflux (i.e., 0.06 atoms/s) is depleting through a slanted grain boundary given that the top interface is blocked by the cobalt cap. Clearly, the void maintains its symmetric morphology during

growth and is unaffected by the grain boundary. This can be explained by the relatively small ion depletion rate from the void and also the strong impact of surface energy given the void length-scale in a merely 44 nm thick wire, which results in fast

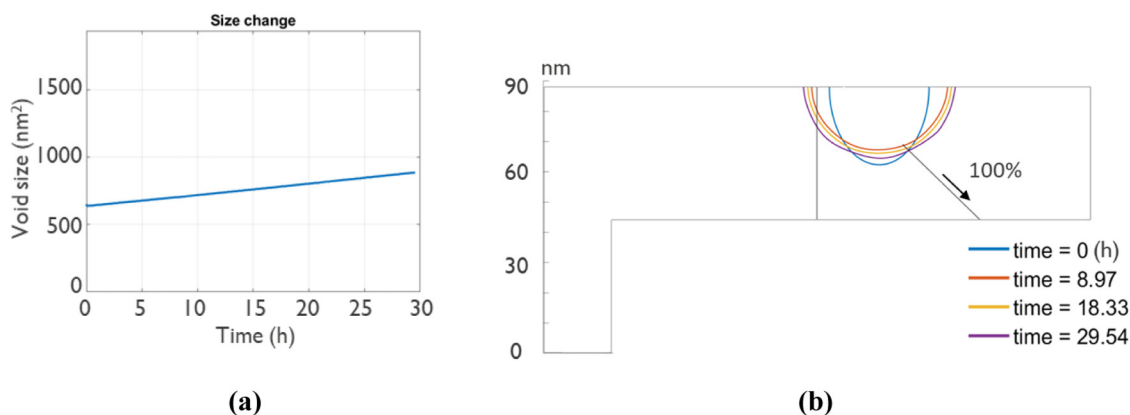


FIG. 14. (a) Void growth with time as determined by the global model for a $100\text{-}\mu\text{m}$ long line with a thickness of 44 nm with cobalt cap (b) void evolution at the local level near cathode assuming the 100% of the ion flux (i.e., 0.06 atoms/s) is depleting through the slanted grain boundary (see video “Case 6.1.avi” of the [supplementary material](#)).

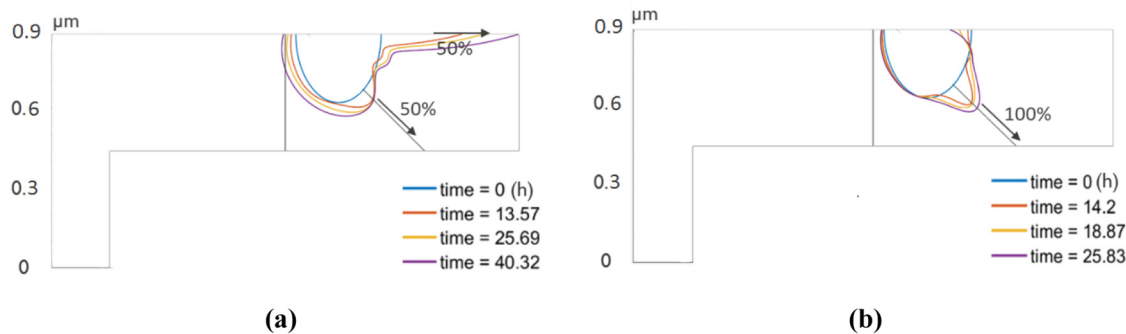


FIG. 15. Void growth pattern for a 440 nm thick interconnect with an ion flux of 12 atoms/s (a) void evolution assuming 50% of the ion outflux is depleting through the slanted grain boundary and 50% through the cap interface (b) void evolution assuming 100% of the ion outflux is depleting through the slanted grain boundary (see video “Case 6.2.avi” of the [supplementary material](#)).

redistribution of atoms over the void surface to minimize the Laplacian of void surface curvature and thereby the chemical potential energy. This is best demonstrated in [Fig. 15](#) where the ion depletion rate from the void is increased by 200 folds (i.e., 12 atoms/s) and also the wire thickness and void size are up-scaled 10 folds (i.e., $S = 10$). Under the latter conditions, the void extends toward the fast diffusion paths depending on the contribution of each fast diffusion path (i.e., grain boundary, cap interface) to the ion depletion rate. In [Fig. 15\(a\)](#), the slanted grain boundary and the top interface contribute equally to the depletion rate, thereby causing an extension of the void along both of the paths. In contrast, in [Fig. 15\(b\)](#), all the outflux is depleting from the slanted grain boundary leading to void elongation along the grain boundary only.

VI. MODEL CORROBORATION

In this section, all the incorporated capabilities of the modeling framework as showcased in previous sections are employed in order to simulate the experimentally observed void dynamic patterns in [Ref. 30](#). The simulation parameters are chosen based on the electromigration conditions and interconnect geometrical parameters in [Ref. 30](#) in which electromigration tests were conducted together with top-down *in situ* scanning electron microscopy (SEM) to monitor void evolution.

The local 2D model was adapted to capture the void dynamics from a top-down perspective instead of the side view perspective in the case studies and the simulation domain dimensions were modified (i.e., $W = 800$ nm). This is consistent with the nature of the tested interconnects in [Ref. 30](#) which were devised to be wide and thin to facilitate *in situ* monitoring by top-down SEM. The initial void radius was set to $r_0 = 310$ nm (consistent with the void volume plot in [Ref. 30](#), $j_{\text{wire}} = 2$ MA/cm², $\frac{d\sigma}{dx} = \frac{d\sigma}{dy} = 0$, $T = 300$ °C). From the experimental void growth rate, an ion depletion rate of 60 atoms/s was deducted. Anisotropic diffusivity parameter in every grain [$m = 500$, $n = 4$ in Eq. (19)], were assigned to be consistent with values reported in [Ref. 19](#) for $T = 300$ °C.

Full details of crystallographic metrics especially on the lattice orientation of grains and grain boundaries were not readily

available. Given that in the case studies the copper texture was identified as the main knob, in the corresponding simulations the texture was varied to determine if copper texture heterogeneity can predict void morphology variations in [Ref. 30](#). Given the straight geometry of the interconnect, the main factor that can contribute to such drastic void shape variations is the heterogeneity of texture. In [Fig. 16](#), the simulation results are shown where the copper texture and crystal orientation, θ_0 , were tailored to reproduce the

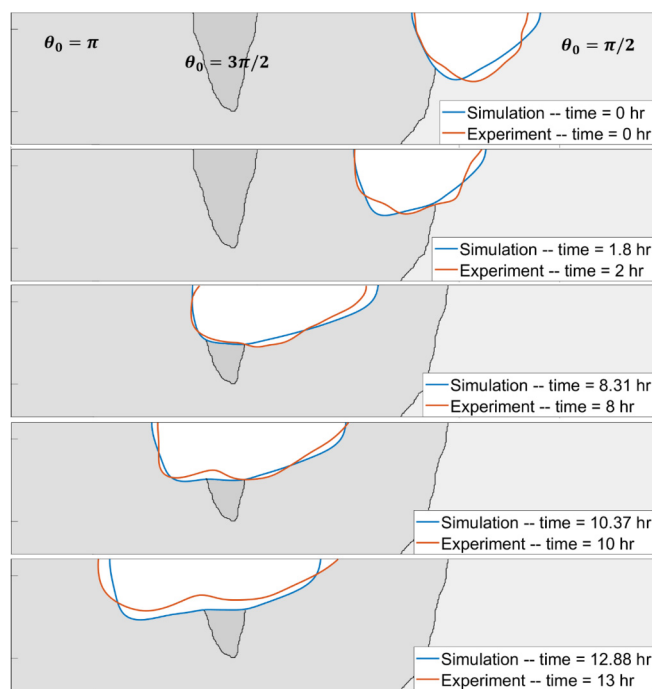


FIG. 16. Simulation results where the copper texture and crystal orientation, θ_0 , were tailored to reproduce the experimental void evolution (see video “Model corroboration.avi” of the [supplementary material](#)).

experimentally observed evolutions, which confirms the key role of the copper texture. Obviously, in the absence of experimental details on the copper texture, it is perilous to claim that the deciphered microstructure details in the simulation are strictly unique. However, the assumed crystal orientations agree with experimental findings in terms of void evolution (see Fig. 16), and they were determined based on an exhaustive iterative study which determined void morphology for every crystal orientation as the crystal was rotated in small increments. This clearly underpins the significant role of copper texture in electromigration, where the models demonstrate that by only rotating the crystal orientation, drastic variations in morphology and, therefore, in electrical resistance and interconnect lifetime can be expected. This also supports the use of our exhaustive approach for modeling of local diffusivity as a distributed function over the void surface instead of the widely used approaches in which a single effective value for diffusivity is employed.

VII. CONCLUSION

In this study, a multi-scale electromigration modeling approach is presented where a 1D Korhonen-type electromigration model determines void volume evolution with time, and a 2D local model simulates void dynamics close to the cathode end of interconnect, considering the impact of (i) electrical current (ii) stress-gradients (iii) copper texture and anisotropic diffusivity of the FCC lattice. Void morphology, size, migration, and local electrical resistance evolution are among the outputs of the modeling framework. Impact of length-scale in the context of void dynamics was studied, where it was found that stress migration is length-scale independent. In stark contrast, a 10-fold increase of migration velocity was observed by 10-fold dimensional downscaling for an iso-volume void under the impact of electrical current. Voids migrated toward higher stress gradients, irrespective of being compressive or tensile and the initial location of the void determined the voids preference in terms of migration direction, i.e., up or down the stress gradients. Stress gradients across interconnect thickness were shown to facilitate slit morphology. Cu texture was identified as the dominant factor in void dynamics. Surface diffusivity in copper is a strong function of surface orientation such that $D_{s111} > D_{s100} > D_{s110}$, and the absolute values differ by several orders of magnitude, i.e., $10^{-6} > 10^{-10} > 10^{-12}$ respectively at 150 °C. This renders copper texture and the orientation of FCC lattice with respect to the longitudinal axis of the interconnect to be the key parameter determining the fate of a void. Such strong anisotropy leads to faceted morphology of voids, and a 40% increase of migration velocity was shown by 45° rotation of copper grain lattice. As such, the model lends itself to use for texture engineering and optimization for electromigration performance and can be used to better understand some of the fundamental causes of electromigration lifetime variability.

SUPPLEMENTARY MATERIAL

See the [supplementary material](#) for the detailed derivation of the void's critical radius and the scaling effect on void migration speed under longitudinal stress.

DATA AVAILABILITY

The data that support the findings of this study are available within the article and its [supplementary material](#).

REFERENCES

- ¹M. A. Korhonen *et al.*, "Microstructure based statistical model of electromigration damage in confined line metallizations in the presence of thermally induced stresses," *J. Appl. Phys.* **74**(8), 4995–5004 (1993).
- ²A. Oates, "Strategies to ensure electromigration reliability of Cu/low-k interconnects at 10 nm," *ECS J. Solid State Sci. Technol.* **4**(1), 3168–3176 (2014).
- ³S. Choi *et al.*, "Effect of metal line width on electromigration of BEOL Cu interconnects," in *IEEE International Reliability Physics Symposium (IRPS)* (IEEE, Burlingame, CA, 2018), pp. 4F.4-1–4F.4-6.
- ⁴K. Croes *et al.*, "Reliability mechanisms and lifetime extrapolation methods for scaled interconnect technologies," in *IEEE International Interconnect Technology Conference and 2015 IEEE Materials for Advanced Metallization Conference (IITC/MAM, IEEE, 2015)*, pp. 295–298.
- ⁵K. Croes, "Study of void formation kinetics in Cu interconnects using local sense structures," in *2011 International Reliability Physics Symposium* (IEEE, 2011).
- ⁶J. R. Black, "Electromigration—A brief survey and some recent results," *IEEE Trans. Electron Devices* **16**(4), 338–347 (1969).
- ⁷C. M. Tan and A. Roy, "Electromigration in ULSI interconnects," *Mater. Sci. Eng.* **58**(1–2), 1–75 (2007).
- ⁸K. Vanstreels *et al.*, "In-situ scanning electron microscope observation of electromigration-induced void growth in 30 nm pitch Cu interconnect structures," *J. Appl. Phys.* **115**(7), 074305 (2014).
- ⁹C. Witt *et al.*, "Electromigration: Void dynamics," *IEEE Trans. Device Mater. Reliab.* **16**(4), 446–451 (2016).
- ¹⁰E. Arzt, O. Kraft, W. D. Nix, and J. E. Sanchez, "Electromigration failure by shape change of voids in bamboo lines," *J. Appl. Phys.* **76**(3), 1563–1571 (1994).
- ¹¹D. R. Fridline and A. F. Bower, "Influence of anisotropic surface diffusivity on electromigration induced void migration and evolution," *J. Appl. Phys.* **85**(6), 3168–3174 (1999).
- ¹²D. Maroudas and M. Rauf Gungor, "Continuum and atomistic modeling of electromechanically-induced failure of ductile metallic thin films," *Comput. Mater. Sci.* **23**(1–4), 242–249 (2002).
- ¹³A. F. Bower and S. Shankar, "A finite element model of electromigration induced void nucleation, growth and evolution in interconnects," *Modell. Simul. Mater. Sci. Eng.* **15**(8), 923–940 (2007).
- ¹⁴A. Averbuch, M. Israeli, I. Ravve, and I. Yavneh, "Computation for electromigration in interconnects of microelectronic devices," *J. Comput. Phys.* **167**(2), 316–371 (2001).
- ¹⁵D. N. Bhate, A. Kumar, and A. F. Bower, "Diffuse interface model for electromigration and stress voiding," *J. Appl. Phys.* **87**(4), 1712–1721 (2000).
- ¹⁶H. Zahedmanesh, *et al.*, "Investigating the electromigration limits of Cu nano-interconnects using a novel hybrid physics-based model," *J. Appl. Phys.* **126**(5), 055102 (2019).
- ¹⁷S. Choi, "Effect of metal line width on electromigration of BEOL Cu interconnects," in *2018 IEEE International Reliability Physics Symposium (IRPS)* (IEEE, 2018), p. 4.
- ¹⁸H. Zahedmanesh, O. Varela Pedreira, C. Wilson, Zs. Tókei, and K. Croes, "Copper electromigration: Prediction of scaling limits," in *Proceedings of IEEE International Interconnect Technology Conference (IITC)* (IEEE, 2019).
- ¹⁹P. M. Agrawal, B. M. Rice, and Donald L. Thompson, "Predicting trends in rate parameters for self-diffusion on FCC metal surfaces," *Surf. Sci.* **515**(1), 21–35 (2002).
- ²⁰O. Kraft and E. Arzt, "Electromigration mechanisms in conductor lines: Void shape changes and slit-like failure," *Acta Mater.* **45**(4), 1599–1611 (1997).
- ²¹W. Wang, Z. Suo, and T.-H. Hao, "A simulation of electromigration-induced transgranular slits," *J. Appl. Phys.* **79**(5), 2394–2403 (1996).

- ²²R. Goldman, "Curvature formulas for implicit curves and surfaces," *Comput. Aided Geom. Des.* **22**(7), 632–658 (2005).
- ²³S. P. Hau-Riege and C. V. Thompson, "The effects of the mechanical properties of the confinement material on electromigration in metallic interconnects," *J. Mater. Res.* **15**, 1797–1802 (2000).
- ²⁴M. McLean, "Determination of the surface energy of copper as a function of crystallographic orientation and temperature," *Acta Metall.* **19**, 387 (1971).
- ²⁵K. N. Tu, "Recent advances on electromigration in very-large-scale-integration of interconnects," *J. Appl. Phys.* **94**(9), 5451–5473 (2003).
- ²⁶H. Wang, X. X. Zhonghua, and J. Sun, "Effects of stress and temperature gradients on the evolution of void in metal interconnects driven by electric current and mechanical stress," *Modell. Simul. Mater. Sci. Eng.* **14**, 607 (2006).
- ²⁷H. Zahedmanesh, P. R. Besser, C. J. Wilson, and K. Croes, "Airgaps in nano-interconnects: Mechanics and impact on electromigration," *J. Appl. Phys.* **120**, 095103 (2016).
- ²⁸James R. Rice and Tze-Jer Chuang, "Energy variations in diffusive cavity growth," *J. Am. Ceram. Soc.* **64**, 46–53 (1981).
- ²⁹D. Tio Castro, R. J. O. M. Hoofman, J. Michelon, D. J. Gravesteijn, and C. Bruynseraede, "Void growth modeling upon electromigration stressing in narrow copper lines," *J. Appl. Phys.* **102**, 123515 (2007).
- ³⁰C. Witt, V. Calero, C. K. Hu, and G. Bonilla, "Electromigration: Void dynamics," *IEEE Trans. Device Mater. Reliab.* **16**, 446–451 (2016).